Journal of Colloid and Interface Science 458 (2015) 53–61

Contents lists available at ScienceDirect

Journal of Colloid and Interface Science

journal homepage: www.elsevier.com/locate/jcis

The impact of trough geometry on film shape. A theoretical study of droplets containing polymer, for P-OLED display applications

Adam D. Eales [a], Nick Dartnell [b], Simon Goddard [b], Alexander F. Routh [a,*]

[a] Department of Chemical Engineering, University of Cambridge, Cambridge CB2 3RA, United Kingdom
[b] Cambridge Display Technology Ltd. (Company number 02672530), Godmanchester PE29 2XG, United Kingdom

HIGHLIGHTS

- Deeper trough leads to enhanced coffee-ring formation.
- Steeper banks promote coffee-ring formation.
- Simple way to control final film shape with substrate machining.

GRAPHICAL ABSTRACT

Trough shape affects the final film profile. The influence of the basin depth and the slope of the bank are investigated. The sketch below is not to scale.

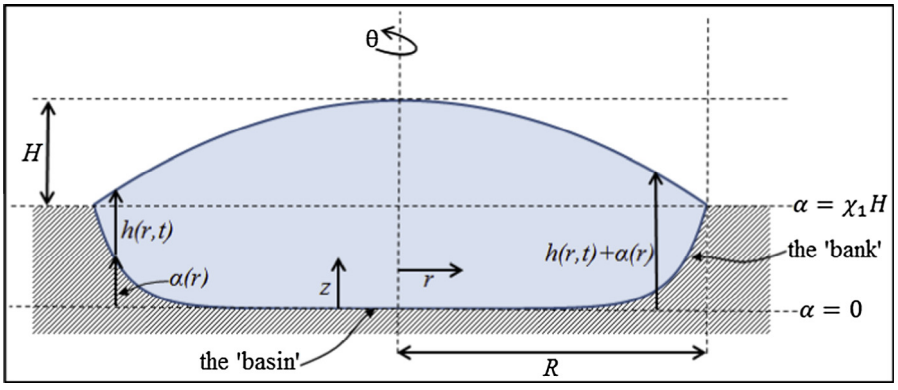

ARTICLE INFO

Article history:
Received 10 June 2015
Revised 14 July 2015
Accepted 14 July 2015
Available online 15 July 2015

Keywords:
Film drying
Droplet
Coffee-ring
Film formation

ABSTRACT

For P-OLED display fabrication, it is important to control the final film shape, arising from drying of volatile droplets containing polymer. Due to peripheral pinning and subsequent outward capillary flow, a coffee-ring typically develops. This is inconvenient since a spatially uniform height, above the substrate, is required to ensure uniform current across the device. Typically the droplets are deposited inside a trough-like structure on the substrate. We present a thin-film lubrication model that tracks the drying dynamics through to the final film shape. The governing equations are derived and solved numerically. We investigate the effect of the trough's depth and the slope of the walls. Increasing the depth or the wall's gradient increases coffee-ring formation. This is due to an increase in horizontal velocity, caused by the substrate's shape as well as delayed gelation of the polymer. The latter allows the outward capillary flow to act for a longer time, before the height becomes fixed.

1. Introduction

There is significant interest in, and research into, the drying of volatile liquid droplets containing polymer, or other non-volatile species. This is due to the array of industrial and practical applications for which drying is an important step. There are several applications for biological fluids [1], including pattern analysis of dried blood, for crime scene investigation [2] and disease diagnostics [3], DNA microarrays [4–7] and herbicides/pesticides on leaves [8]. In addition, micro/nano electronics can be manufactured [9–14] using inkjet printing, as can polymer-organic light-emitting

* Corresponding author.
E-mail address: afr10@cam.ac.uk (A.F. Routh).

http://dx.doi.org/10.1016/j.jcis.2015.07.036
0021-9797/

diode displays (P-OLEDs) [15]. The latter is the focus of this research.

It has long been observed that a ring stain can form in the bottom of a coffee mug. This is common, not only for coffee but for many other systems in which a volatile liquid evaporates, leaving behind a non-volatile solute. The mechanism for this behaviour was identified by Deegan et al. [16–18] and is termed the coffee-ring effect. The edge of the droplet can pin either due to the presence of large particles, as in coffee, or due to surface roughness or adsorption of the non-volatile material to the substrate. The result is an outward capillary flow that acts to replenish liquid material evaporated at the edge. This can transport the non-volatile species outward, where it is deposited as a ring.

For many applications, a ring-like shape is undesirable. Instead, it is desired that the coffee-ring effect is mitigated, to achieve a spatially uniform film. Methods which have been shown to at least reduce the extent of coffee-ring formation are in abundance. A surfactant can be introduced to initiate a Marangoni flow that counteracts the capillary flow [8,19]. An electric field can be chosen to tailor film shape, as shown by Wray et al. [20]. Changing the pH [21,22] can introduce an attraction to the substrate for the non-volatile species. The edge pinning can be prevented, with the droplet edge oscillating due to electrowetting [23]. The use of different particle shapes [22,24,25], can also prevent coffee-ring formation. Nonetheless, the above methods are not ideal for P-OLED applications, because of the introduction of extra components.

The prediction of film shape resulting from droplets containing polymer, is a topic of significant research. For comprehensive reviews, see Larson [26] or Routh [27]. The majority of literature to-date has focused on droplets residing on a flat substrate. These include several models based on thin-film lubrication theory [1,20,28–31]. By contrast, work on non-uniform substrates remains relatively untouched. Studies on soft or deformable substrates exist, for example Lopes and Bonaccurso [32] who find that depinning of water droplets occurs much later if the substrate is soft. There are also some experimental investigations on polymer film shape, such as Kajiya et al. [19] and Jung et al. [14]. The former introduces a Marangoni flow by addition of a surfactant. The latter considers the effect of initial polymer loading and droplet volume. Both papers consider a perfectly rectangular trough. To our knowledge the only theoretical investigation of film shape in typical trough-like geometries, common in P-OLEDs, is that of Okuzono et al. [33]. This again considers the limit of a perfectly rectangular trough and provides a series of analytical expressions and numerical predictions in a cartesian coordinate system. Two groups are examined in the zero capillary number limit; the initial polymer loading and the relative height of the bank to the initial height of the film. With a smaller polymer loading or a larger relative bank height, the coffee-ring effect is increased.

In this paper we aim to examine how the substrate geometry can be tailored to influence the final polymer profile, deposited by evaporating droplets. Whilst we predominantly examine the effect of the trough depth and bank slope for non-rectangular troughs, the model can be used to investigate any substrate shape. Additionally, our model can deal with the influence of finite capillary number, various polymer loadings and diffusion, the extent of evaporation from gelled regions and non-uniform evaporation profiles.

2. Mathematical model

2.1. Assumptions and simplifications

Consider a droplet containing a polymer with initial volume fraction, ϕ_0. The liquid is volatile with volumetric evaporative flux per unit area E_0, density ρ_0, viscosity μ_0, and air/liquid surface tension γ_0. The droplet resides in a trough, impregnated in an otherwise flat, horizontal substrate. Fig. 1 shows a sketch of the droplet. To describe the geometry, we define the height of the substrate to be $\alpha(r)$. This is relative to a reference height, $\alpha = 0$, at the deepest extremity of the trough. The height of the droplet surface above the substrate is termed, $h(r)$. The absolute height of the droplet surface is, therefore, $h(r) + \alpha(r)$. The centre of the trough is typically a horizontal basin at $\alpha = 0$. Away from the basin, there is an increase in α, when moving radially outwards; this region is called the bank. At the edge of the trough, the substrate flattens to a fixed height $\chi_1 H$, where χ_1 is a measure for the trough depth.

The contact line is assumed to pin and remain pinned throughout the drying process. It is assumed that this occurs at the location where the bank meets the flat, trough exterior, at radius R.

The coordinate system is cylindrical, with horizontal position r, vertical position z and azimuthal angle θ. The droplet is taken to be axisymmetric, which enables the azimuthal velocity and differentials in the azimuthal direction to be neglected $\left(v_\theta = 0, \frac{\partial}{\partial\theta} = 0\right)$.

The governing equations are cast into non-dimensional form using the scalings shown in Table 1. The original height of the droplet above the top of the trough is taken as H. Henceforth, all non-dimensional properties are denoted with an overscore.

Several dimensionless numbers can be estimated following the scaling analysis. Typical parameter values are $H = 10\,\mu\text{m}$, $R = 125\,\mu\text{m}$, $\rho_0 = 1084\,\text{kg m}^{-3}$, $\mu_0 = 1.8 \times 10^{-3}\,\text{N s m}^{-2}$, $\gamma_0 = 3.7 \times 10^{-2}\,\text{N m}^{-1}$, $E_0 = 2.0 \times 10^{-9}\,\text{m}^3\,\text{m}^{-2}\,\text{s}^{-1}$, the diffusivity of polymer, D_0, is taken as $1.2 \times 10^{-12}\,\text{m}^2\,\text{s}^{-1}$. The liquid properties are for methyl benzoate at standard temperature and pressure [34] and the evaporation rate was determined by weighing the mass loss from a petri dish containing methyl benzoate. The diffusion coefficient is calculated for 100 nm rigid spheres in methyl benzoate.

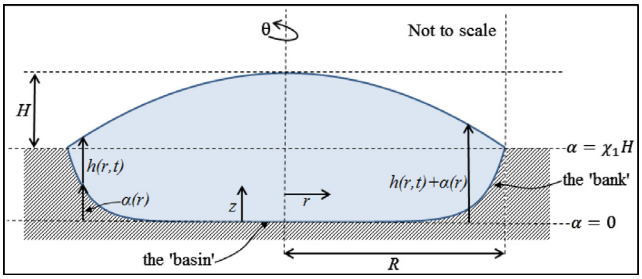

Fig. 1. Sketch of a droplet in the trough geometry.

Table 1
Scaling terms used.

Property	Scaling term
Substrate height, α	H
Droplet height above substrate, h	H
Vertical position, z	H
Horizontal position, r	R
Vertical velocity, v_z	E_0
Horizontal velocity, v_r	RE_0/H
Viscosity, μ	μ_0
Surface tension, γ	γ_0
Density, ρ	ρ_0
Pressure, p	$\mu_0 R^2 E_0/H^3$
Time, t	H/E_0

$$Bo = \frac{\rho_0 g R^2}{\gamma_0} \sim 10^{-3} \tag{1}$$

$$Re = \frac{\rho_0 E_0 R}{\mu_0} \sim 10^{-7} \tag{2}$$

$$Ca = \frac{3\mu_0 R^4 E_0}{\gamma_0 H^4} \sim 10^{-6} \tag{3}$$

$$Pé = \frac{R^2 E_0}{H D_0} \approx 3 \tag{4}$$

The Bond number, *Bo*, represents the relative importance of gravitational and surface tension effects on the droplet. Since it is small, gravitational effects can be ignored. The Reynolds number, *Re*, is the ratio of inertial to viscous forces. Since it is very small, the inertial terms in the Navier–Stokes equations can be ignored. Furthermore, we consider the case of thin droplets, such that $Re \cdot \frac{H^2}{R^2} \ll 1$. In this regime, the lubrication approximation can be applied. The small capillary number, *Ca*, implies that surface tension effects dominate over viscous effects. The Péclet number, *Pé*, relates the rate of convection to polymer diffusion. Typically polymer diffusion is weak. In previous work [36] it has been shown that weak diffusion can slightly reduce the extent of coffee-ring formation. This subtlety is not the focus of this research. For this reason the Péclet number is taken to be infinite such that polymer diffusion is ignored.

With regard to the polymer, it is initially distributed homogeneously, with volume fraction ϕ_0 at all locations. The polymer fraction will increase as the volatile liquid evaporates. However, a maximum polymer volume fraction, ϕ_{max}, will exist, due to the onset of polymer gelation. As the polymer volume fraction increases, the dispersion viscosity will increase. This is modelled by the expression in Eq. (5), following Krieger and Dougherty [35].

$$\mu = \mu_0 g(\phi) = \mu_0 \left[1 - \frac{\phi}{\phi_{max}}\right]^{-n} \tag{5}$$

The constant, *n*, accounts for the rate of increase in viscosity with volume fraction.

The surface tension of the liquid can also be influenced by the increase in polymer volume fraction. If necessary, this can be accounted for by using a surface tension correction function. For inks that interest us, however, we find there to be minimal impact and so the approximation that surface tension is not affected by the presence of polymer is reasonable.

Due to evaporation of the volatile liquid and pinning of the contact line, a gelled region forms at the edge with volume fraction, ϕ_{max}. The works of Tarasevich et al. [1] and Ozawa et al. [28], on flat substrates, assumed that this gelation completely suppresses all evaporation from this region. It is worth noting that we do not observe wet films following completion of evaporation. Therefore, whilst evaporation will be significantly hindered by polymer gelation, it cannot be completely suppressed. Following our previous works [36,37], we account for this by using an evaporation suppression factor, f_h. This adjusts the evaporation rate in the gelled region as shown in Eq. (6). This subtlety is not the focus of this paper, so f_h is taken to be unity.

$$\text{In the close-packed region}: \; E_h(r) = (1 - f_h)E(r), \quad \text{where } 0 \leqslant f_h \leqslant 1 \tag{6}$$

For the purposes of this paper, the evaporative flux distribution is taken as spatially uniform ($E = E_0 \neq f(r)$). If necessary, this model could be extended to account for edge-enhanced evaporation modes. Our previous work [36] showed that inclusion of the spatially varying evaporation has only a small influence on the final film profile.

2.2. Derivation methodology and governing equations

The governing equations for the change in droplet height and polymer volume fraction with position and time have previously been derived for flat substrates [1,20,28,30,31] and for perfectly rectangular troughs in cartesian coordinates [33]. Here we extend our work [36] to account for the trough geometry.

The change in droplet height and polymer volume fraction, with position and time, both depend on the internal flow profile. Specifically, for thin droplets in the lubrication regime, it is the horizontal velocity, v_r, that influences the dynamics. To find an expression for the horizontal velocity, we start with the Navier–Stokes equations. Using the lubrication approximation, one finds that the pressure gradient in the vertical direction is negligible. The horizontal velocity is then determined by

$$\frac{\partial^2 \bar{v}_r}{\partial \bar{z}^2} = \frac{1}{g(\phi)} \frac{d\bar{p}}{d\bar{r}} \tag{7}$$

Eq. (7) can be integrated twice (assuming $\phi \neq \phi(\bar{z})$), subject to zero-shear at the droplet surface $\left(\frac{\partial \bar{v}_r}{\partial \bar{z}} = 0 \text{ at } \bar{z} = \bar{h} + \bar{\alpha}, \text{ for thin droplets}\right)$ and no slip along the substrate ($\bar{v}_r = 0$ at $\bar{z} = \bar{\alpha}$). The result is an expression for the horizontal velocity as a function of the horizontal pressure gradient, the vertical position and the height of the substrate and the droplet, above the substrate.

$$\bar{v}_r = \frac{\bar{z}^2 - 2(\bar{h} + \bar{\alpha})\bar{z} + 2\bar{h}\bar{\alpha} + \bar{\alpha}^2}{2g(\phi)} \frac{d\bar{p}}{d\bar{r}} \quad \bar{\alpha} \leqslant \bar{z} \leqslant \bar{h} + \bar{\alpha} \tag{8}$$

Since depthwise gradients are negligible it makes more sense to use a vertically averaged radial velocity, $\tilde{\bar{v}}_r$.

$$\tilde{\bar{v}}_r = \frac{1}{\bar{h}} \int_{\bar{z}=\bar{\alpha}}^{\bar{z}=\bar{h}+\bar{\alpha}} \bar{v}_r d\bar{z} = -\frac{\bar{h}^2}{3g(\phi)} \frac{d\bar{p}}{d\bar{r}} \tag{9}$$

The horizontal pressure gradient term is determined from the Young–Laplace equation ($p = -\gamma\kappa$), which relates the surface pressure, *p*, to the surface tension, γ and the droplet's mean curvature, κ. Using the lubrication approximation one obtains

$$\bar{p} = -\frac{\gamma_0 H^4}{\mu_0 R^4 E_0} \left(\frac{\partial^2 (\bar{h} + \bar{\alpha})}{\partial \bar{r}^2} + \frac{1}{\bar{r}} \frac{\partial (\bar{h} + \bar{\alpha})}{\partial \bar{r}} \right) \tag{10}$$

Through differentiation of this and subsequent substitution into Eq. (9), the vertically averaged horizontal velocity is

$$\tilde{\bar{v}}_r = \frac{\bar{h}^2}{Ca\, g(\phi)} \left[\frac{\partial^3 \bar{h}}{\partial \bar{r}^3} + \frac{\partial^3 \bar{\alpha}}{\partial \bar{r}^3} + \frac{1}{\bar{r}} \left(\frac{\partial^2 \bar{h}}{\partial \bar{r}^2} + \frac{\partial^2 \bar{\alpha}}{\partial \bar{r}^2} \right) - \frac{1}{\bar{r}^2} \left(\frac{\partial \bar{h}}{\partial \bar{r}} + \frac{\partial \bar{\alpha}}{\partial \bar{r}} \right) \right] \tag{11}$$

where $Ca = \frac{3\mu_0 R^4 E_0}{\gamma_0 H^4}$ is the capillary number.

Eq. (11) differs from the flat substrate expression, because of the inclusion of the $\bar{\alpha}$ terms. The substrate geometry affects the horizontal pressure gradient and therefore, the internal flow profile.

The governing partial differential equations for droplet height and polymer volume fraction can be similarly found. Provided that the substrate is not soft, so that $\bar{\alpha}$ is independent of time, the governing equations do not differ compared with the flat substrate case. The effect of the substrate geometry appears in the expression for the horizontal velocity, $\tilde{\bar{v}}_r$.

$$\frac{\partial \bar{h}}{\partial \bar{t}} = -\bar{E}(\bar{r}) - \frac{1}{\bar{r}} \frac{\partial}{\partial \bar{r}} \left[\bar{r} \bar{h} \tilde{\bar{v}}_r \right] \tag{12}$$

$$\frac{\partial \phi}{\partial \bar{t}} = \frac{\phi \bar{E}(\bar{r})}{\bar{h}} - \tilde{\bar{v}}_r \frac{\partial \phi}{\partial \bar{r}} + \frac{Pé^{-1}}{\bar{r}\bar{h}} \frac{\partial}{\partial \bar{r}} \left[\bar{r} \bar{h} \frac{\partial \phi}{\partial \bar{r}} \right] \tag{13}$$

where $\bar{E}(\bar{r})$ is the dimensionless form of the evaporative flux distribution, which in this work is taken as a constant.

2.3. Modeling the substrate geometry

In order to generate a numerical solution it is necessary to assume a function for the substrate height. As can be seen in Eq. (11), the horizontal velocity depends on the spatial derivatives of this function. If there were a step change in either the substrate height or the gradient of the substrate, numerical issues would occur.

In practice, the centre of the trough is typically a horizontal basin and the walls slope inward in a so-called 'bank'. There are two interesting parameters to study, the depth of the basin and the extent of the bank. A measure for the latter could either be the gradient of the bank or the distance that it protrudes into the trough. Eq. (14) is used to provide a continuous function for the substrate height, within the trough. The external substrate height is fixed, as shown by Eq. (15)

$$\bar{\alpha}(\bar{r}) = \chi_1\left[\tanh^{-1}(\bar{r}\tanh(1))\right]^{\chi_2} \quad \text{for } 0 \leqslant \bar{r} < 1 \tag{14}$$

$$\bar{\alpha}(\bar{r}) = \chi_1 \quad \text{for } \bar{r} \geqslant 1 \tag{15}$$

The parameter χ_1 is a measure for the trough depth. For larger χ_1, the trough is deeper. The extent of the bank is controlled by χ_2. For larger χ_2, the bank is more confined to the periphery of the trough and has steeper gradient. Figs. 2 and 3 show plots of Eq. (14) for varying χ_1 and χ_2 respectively.

2.4. Boundary and initial conditions

The boundary conditions at the centreline are symmetry and zero flux.

$$\frac{\partial(\bar{h}+\bar{\alpha})}{\partial\bar{r}} = 0 \quad \& \quad \bar{r}\bar{h}\tilde{\bar{v}}_r = 0 \quad \text{at } \bar{r} = 0 \tag{16}$$

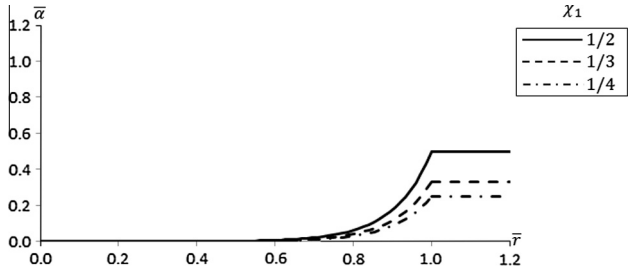

Fig. 2. Substrate profile $\bar{\alpha}(\bar{r})$ as a function of the trough depth parameter, χ_1. In this example χ_2 is taken as $\chi_2 = 6$.

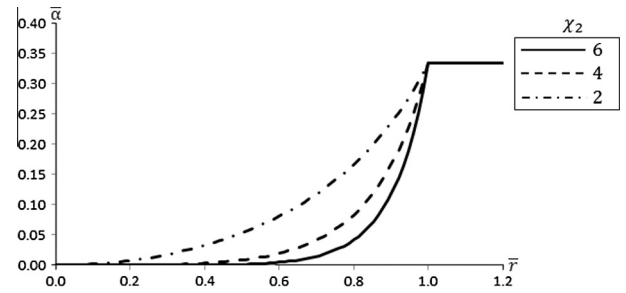

Fig. 3. Substrate profile $\bar{\alpha}(\bar{r})$ as a function of the bank extent parameter, χ_2. In this example χ_1 is taken as $\chi_1 = 1/3$.

At the edge of the droplet the height above the substrate is zero and the horizontal velocity is zero, since the droplet remains pinned.

$$\bar{h} = 0 \quad \& \quad \tilde{\bar{v}}_r = 0 \quad \text{at } \bar{r} = 1 \tag{17}$$

When the polymer volume fraction has increased, to the extent that a gelled region forms, the partial differential Eqs. (12) and (13) can only be solved in the liquid region. This necessitates a change to the outer boundary conditions. At the location of the liquid/gel boundary, $\bar{r}_f$, we say

$$\bar{h} = \bar{h}_f \quad \& \quad \tilde{\bar{v}}_r\big|_{\bar{r}=\bar{r}_f} = \frac{(1-f_h)\int_{\bar{r}_f}^{1}\bar{r}\bar{E}(\bar{r})d\bar{r}}{\bar{r}_f\bar{h}_f} \quad \text{at } \bar{r} = \bar{r}_f \tag{18}$$

where $\bar{h}_f$ and $\tilde{\bar{v}}_r|_{\bar{r}=\bar{r}_f}$ are the height and horizontal velocity at the location of the liquid/gel boundary, respectively. The expression for the horizontal velocity can be evaluated numerically and is zero in the case that $f_h = 1$.

Under certain conditions, the gelation can occur at the centre, as well as the edge. When this occurs the inner boundary conditions for partial differential Eqs. (12) and (13) also need to be changed. In this eventuality, the height and horizontal velocity at the inner gel/liquid boundary, $\bar{r}_{if}$, are set using

$$\bar{h} = \bar{h}_{if} \quad \& \quad \tilde{\bar{v}}_r\big|_{\bar{r}=\bar{r}_{if}} = \frac{-(1-f_h)\int_0^{\bar{r}_{if}}\bar{r}\bar{E}(\bar{r})d\bar{r}}{\bar{r}_{if}\bar{h}_{if}} \quad \text{at } \bar{r} = \bar{r}_{if} \tag{19}$$

where $\bar{h}_{if}$ and $\tilde{\bar{v}}_r|_{\bar{r}=\bar{r}_{if}}$ are the height and horizontal velocity at the inner gel/liquid boundary, respectively.

Once gelation has occurred, the polymer volume fraction ($\phi = \phi_{max}$) and the height are fixed and no longer evolve with time.

The initial shape of the droplet is taken to be a spherical cap. There are two scenarios that one can consider. Either the initial surface shape is fixed, as in Eq. (20) or the initial droplet volume is fixed, as in Eq. (21).

$$\bar{h}(\bar{r},\bar{t}=0) + \bar{\alpha}(\bar{r}) = (1+\chi_1) - \bar{r}^2 \quad \text{for } 0 \leqslant \bar{r} \leqslant 1 \tag{20}$$

$$\bar{h}(\bar{r},\bar{t}=0) + \bar{\alpha}(\bar{r}) = \chi_1 + c(1-\bar{r}^2) \quad \text{for } 0 \leqslant \bar{r} \leqslant 1 \tag{21}$$

where the constant c in Eq. (21) is determined for each χ_1, by ensuring the initial droplet volume is matched to that for the flat substrate case, $\chi_1 = 0$.

$$c = \frac{\int_0^1 2\pi\bar{r}(1-\bar{r}^2)d\bar{r} - \int_0^1 2\pi\bar{r}(\chi_1 - \bar{\alpha}(\bar{r}))d\bar{r}}{\int_0^1 2\pi\bar{r}(1-\bar{r}^2)d\bar{r}} \tag{22}$$

The initial conditions are shown for the fixed initial shape and the fixed initial volume scenarios, in Figs. 4 and 5, respectively.

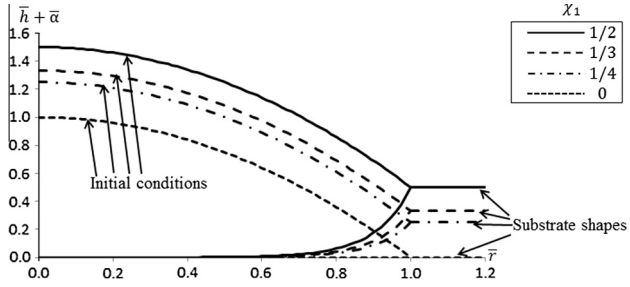

Fig. 4. Sketch to show the initial conditions as a function of the basin depth, χ_1, for the fixed initial shape scenario, following Eq. (20). The plots of the substrate height use Eqs. (14) and (15), with fixed $\chi_2 = 6$ and varying χ_1.

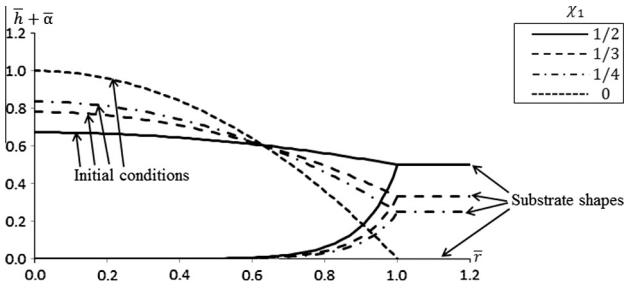

Fig. 5. Sketch to show the initial condition as a function of the basin depth, χ_1, with a fixed initial dimensionless volume of $\pi/2$, following Eqs. (21) and (22). The plots of the substrate height use Eqs. (14) and (15), with fixed $\chi_2 = 6$ and varying χ_1.

2.5. Numerical implementation

Following our previous paper [36], we use a mixed numerical scheme. The change to the spatial derivatives of height is faster than the change in height itself, provided the time-step is small enough. This enables Eq. (12) to be linearised.

At each time-step, the discretised, finite difference scheme is solved using Newton's method. This provides an update to the height and polymer volume fraction profiles.

2.6. Groups that we will consider

The polymer content, diffusion and the magnitude of the capillary number can all contribute. For these, the interested reader may wish to refer to our previous work [36]. In this paper, we solely focus on the impact of the trough geometry on final film shape. The two parameters that we examine are the trough depth χ_1 and the bank extent χ_2, as defined in Eq. (14).

3. Numerical results and discussion

It is not straightforward to develop a measure for how flat the final film is. It might be required that the surface film shape, $(\bar{h}+\bar{\alpha})$, does not undulate. Alternatively, it could be the height above the substrate $\bar{h}$ that needs to be spatially uniform. It depends on the application.

Following previous work on flat substrates [36,37], the measure for the extent of coffee-ring formation, *CR*, will be the ratio of the maximum height of the peripheral ring $\bar{h}_p$ (above the substrate), to the final central height $\bar{h}_c$. If *CR* becomes smaller, the coffee-ring effect is reduced.

$$CR = \frac{\bar{h}_p}{\bar{h}_c} \tag{23}$$

The definitions of $\bar{h}_p$ and $\bar{h}_c$ are sketched in Fig. 6.

For P-OLED display applications it is more appropriate that the film height across the region at the bottom of the trough (i.e. where $\bar{\alpha} \sim 0$) is constant. An alternate form of *CR* would be required however the trends seen and conclusions drawn in this report would be unchanged.

3.1. Influence of the trough depth

The extent to which the trough depth influences the final shape depends on the relative magnitudes of the initial central height $(1+\chi_1)$ and the trough depth χ_1. For small χ_1, the trough is subtle and so its effect is reduced. If χ_1 is larger, it can have an appreciable effect on the final shape.

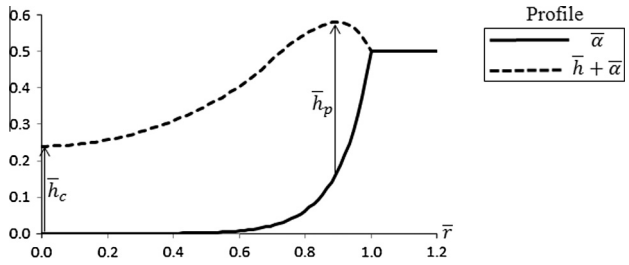

Fig. 6. Sketch of the definitions of the maximum height of the peripheral ring, $\bar{h}_p$, and the final central height, $\bar{h}_c$ for the final $\bar{h}(\bar{r})$ profile.

Neither the fixed shape (Fig. 4) nor the fixed volume (Fig. 5) initial conditions are ideal for making direct comparisons. Either the initial volumes or initial shapes vary as a function of the trough depth. It should be noted however, that no matter which scenario is chosen, there is no qualitative difference in the trends seen with varying trough depth, when considering the measure *CR*. For this reason, the results for the fixed volume initial condition are provided in Supplementary information. The final $\bar{h}(\bar{r})$ profile is shown in Fig. 7 as a function of χ_1, for the fixed shape initial condition. Similarly, the final $\bar{h}(\bar{r})+\bar{\alpha}(\bar{r})$ profile is shown in Fig. 8. The solution for $\chi_1 = 0$ is equivalent to the result for a flat substrate.

For both $\bar{h}(\bar{r})$ and $\bar{h}(\bar{r})+\bar{\alpha}(\bar{r})$ profiles, an increased trough depth results in a larger extent of deposition at the edge and less in the centre.

Comparison of the profiles for the fixed volume initial condition can never be completely fair because the initial droplet shapes and the capillary numbers are different for each value of χ_1. Whilst there is qualitative agreement with the trends seen in Figs. 7 and 8, only the fixed initial shape scenario will be considered in the subsequent quantitative analysis.

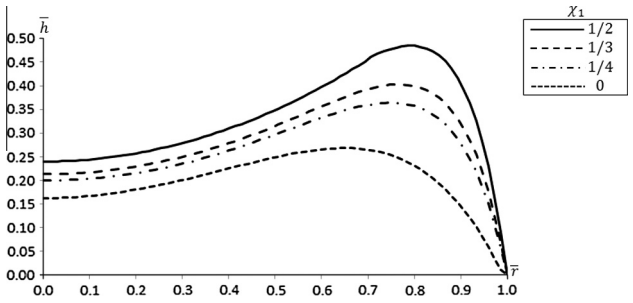

Fig. 7. The final $\bar{h}(\bar{r})$ profile as a function of the trough depth, χ_1. The results are shown for $Ca = 10^{-3}$, $f_h = 1$, $Pe \to \infty$, $\phi_0/\phi_{max} = 0.4$, $\chi_2 = 6$ and the fixed shape initial condition.

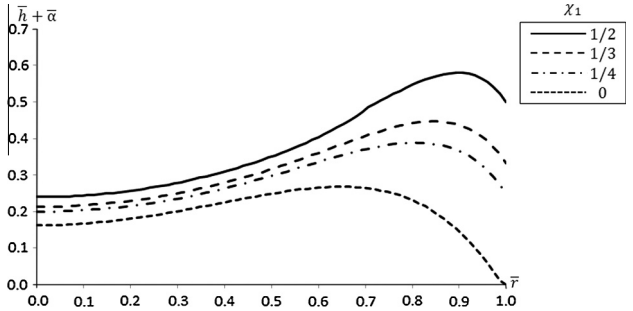

Fig. 8. The final $\bar{h}(\bar{r})++\bar{\alpha}(\bar{r})$ profile as a function of the trough depth, χ_1. The results are shown for $Ca = 10^{-3}$, $f_h = 1$, $Pe \to \infty$, $\phi_0/\phi_{max} = 0.4$, $\chi_2 = 6$ and the fixed shape initial condition.

To enable direct comparison of the profiles in Figs. 7 and 8, rescaling would be required to ensure the total polymer quantity were the same for each basin depth. However, any rescaling would apply to both $\bar{h}_p$ and $\bar{h}_c$. Therefore, the coffee-ring measure *CR* would be unaffected by the rescaling. Since *CR* is the term of interest, the plots in Figs. 7 and 8 are not rescaled.

The measure for the extent of coffee-ring formation in the final $\bar{h}(\bar{r})$ profile is plotted in Fig. 9, as a function of the basin depth. An analogous coffee-ring measure, $CR^{\star}$, is applied to the final $\bar{h}(\bar{r})+\bar{\alpha}(\bar{r})$ profile and is superimposed.

There are two potential causes for the increase in coffee-ring formation with trough depth. The first is due to the flow profile. The horizontal velocity changes due to the spatial derivatives of $\bar{\alpha}$. Eq. (24) shows the change to the horizontal velocity relative to a flat substrate. This alters the quantity of polymer transported to the edge.

$$\Delta\tilde{\bar{v}}_r(\bar{r}) = \frac{\bar{h}^2}{Ca\, g(\phi)}\left[\frac{\partial^3\bar{\alpha}}{\partial\bar{r}^3}+\frac{1}{\bar{r}}\frac{\partial^2\bar{\alpha}}{\partial\bar{r}^2}-\frac{1}{\bar{r}^2}\frac{\partial\bar{\alpha}}{\partial\bar{r}}\right] \tag{24}$$

The surface height above the substrate and the polymer volume fraction both influence the magnitude of $\Delta\tilde{\bar{v}}_r$ and these vary with time and position. Whilst the magnitude of the flow depends on time, the sign does not because $\bar{\alpha}$ is independent of time. To understand the effect the substrate has on the flow profile, the sign of Eq. (24) is important. If $\Delta\tilde{\bar{v}}_r > 0$ the outward velocity is increased and more polymer is transported outwards; the converse is true for $\Delta\tilde{\bar{v}}_r < 0$. The value of $\Delta\tilde{\bar{v}}_r$ is plotted as a function of χ_1 in Fig. 10, at fixed $\chi_2 = 6$.

In all scenarios, $\Delta\tilde{\bar{v}}_r$ is positive at all locations. The substrate geometry leads to an increase in the outward velocity and so aids coffee-ring formation. As χ_1 becomes bigger, this behaviour becomes more pronounced.

The second mechanism that could increase the coffee-ring effect is due to delayed polymer gelation. This is demonstrated in Fig. 11, which shows the rate of the liquid/gel front progression as a function of χ_1 for the fixed shape initial condition. The results for the fixed initial volume scenario qualitatively agree but are not reported for conciseness. With an increase in trough depth, it will take longer for the polymer volume fraction to reach $\phi_{\max}$. This is because as the trough becomes deeper, for a fixed initial shape above the trough, the fluid depth above the substrate is increased. The outward capillary flow has a longer period of time to cause the ring formation, before the height becomes fixed by gelation.

When the trough depth is increased beyond $\chi_1 = 1/2$, the coffee-ring effect continues to become more prominent. However, for $\chi_1 > 1/2$ this trend weakens slightly, as evidenced in Fig. 9 by the very subtle decrease in gradient. The reason for this is that gelation occurs at the centre, before evaporation is complete. The gelation still occurs at the edge, so the result is a liquid domain shrinking from both inner and outer boundaries. The double gelation fixes the height at the centre and accounts for the reduction in the magnitude of the increase in *CR*. The double gelation behaviour becomes more pronounced if the evaporation suppression factor f_h or the polymer content $\phi_0/\phi_{\max}$ are reduced.

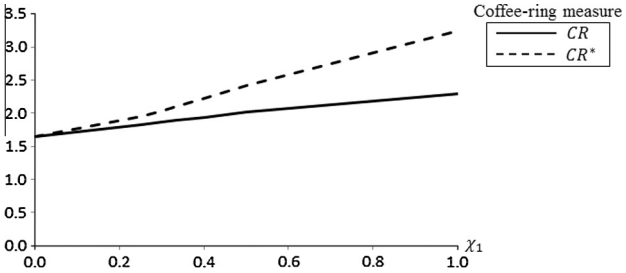

Fig. 9. The coffee-ring measure *CR* for the final $\bar{h}(\bar{r})$ profile as a function of the trough depth, χ_1. An analogous coffee-ring measure, $CR^{\star}$, is applied to the final $\bar{h}(\bar{r})+\bar{\alpha}(\bar{r})$ profile and the results are superimposed for comparison. The results are shown for $Ca = 10^{-3}$, $f_h = 1$, $Pé \to \infty$, $\phi_0/\phi_{\max} = 0.4$, $\chi_2 = 3$ and the fixed shape initial condition.

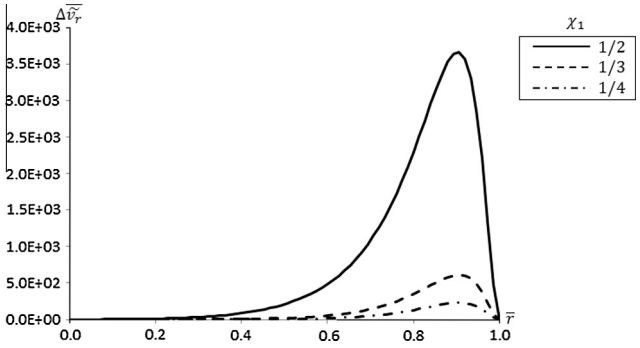

Fig. 10. A plot of the analytical expression for $\Delta\tilde{\bar{v}}_r$, as a function of the trough depth, χ_1. The plots are shown for $Ca = 10^{-3}$, $g(\phi) = 1$, $\bar{h}(\bar{r}) = (1+\chi_1) - \bar{\alpha}(\bar{r}) - \bar{r}^2$ and $\chi_2 = 6$. A positive $\Delta\tilde{\bar{v}}_r$ corresponds to an increase in the outward horizontal velocity.

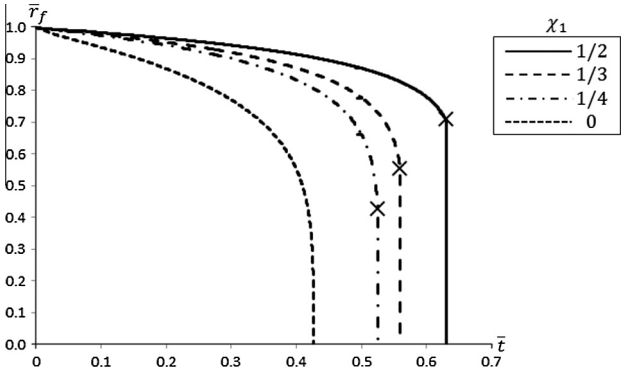

Fig. 11. The progression of the liquid/gel front location, $\bar{r}_f$, as a function of time and the trough depth, χ_1. The symbol $\times$ indicates the position of the original liquid/gel front when the droplet starts to gel at the centre as well. The results are shown for $Ca = 10^{-3}$, $f_h = 1$, $Pé \to \infty$, $\phi_0/\phi_{\max} = 0.4$, $\chi_2 = 6$ and the fixed shape initial condition.

3.2. Influence of the bank extent

In this section the parameter χ_2 is examined at fixed χ_1. Fig. 12 shows the final $\bar{h}(\bar{r})$ profile for various χ_2 at fixed $\chi_1 = 1/3$ and polymer content $\phi_0/\phi_{\max} = 0.4$.

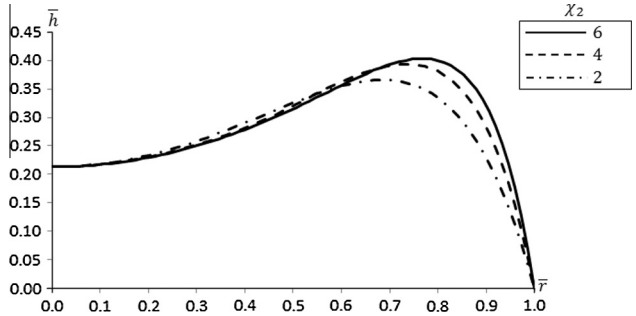

Fig. 12. The final $\bar{h}(\bar{r})$ profile as a function of the bank extent, χ_2. The results are shown for $Ca = 10^{-3}$, $f_h = 1$, $Pé \to \infty$, $\phi_0/\phi_{\max} = 0.4$, $\chi_1 = 1/3$ and the fixed shape initial condition.

With increasing χ_2 the coffee-ring effect becomes more pronounced. The peak position of the ring also shifts further towards the periphery.

Fig. 13 shows the measure for coffee-ring formation for the final $\bar{h}(\bar{r})$ profile, as a function of χ_2. An analogous coffee-ring measure is applied to the final $\bar{h}(\bar{r}) + \bar{\alpha}(\bar{r})$ profile and is superimposed.

For $\chi_1 = 1/3$, the extent of coffee-ring formation in the $\bar{h}(\bar{r}) + \bar{\alpha}(\bar{r})$ profile reaches a maxima when $\chi_2 \approx 1$. If χ_2 is increased further, $CR^\star$ decreases. This is because the substrate height is significantly smaller, so that the peak height in the $\bar{h}(\bar{r}) + \bar{\alpha}(\bar{r})$ profile is reduced. However, the $\bar{h}(\bar{r}) + \bar{\alpha}(\bar{r})$ profiles still show a greater extent of ring formation than for a flat substrate.

The reason for the enhanced coffee-ring effect in the $\bar{h}(\bar{r})$ profile follows a similar argument to that given in the influence of trough depth section. Fig. 14 shows $\Delta\tilde{\bar{v}}_r$ as a function of χ_2 at fixed $\chi_1 = 1/3$.

Again the positive values of $\Delta\tilde{\bar{v}}_r$ indicate an enhanced flow to the edge and hence an additional coffee-ring effect compared to a flat substrate. However, as shown in Fig. 14, the magnitude of $\Delta\tilde{\bar{v}}_r$ is larger when the bank slope is gentle. This trend is in contrast to the result for CR, shown in Fig. 13. It follows that, for the basin depth considered ($\chi_1 = 1/3$), the delayed gelation mechanism must be more important than the change in horizontal velocity caused by the substrate. As illustrated in Fig. 15, the progression of the liquid/gel front is slower when the bank is steeper. The outward capillary flow, therefore, has a longer period of time to cause the ring formation, before the height becomes fixed by gelation.

For small values of $\chi_2 < 1.5$, $\Delta\tilde{\bar{v}}_r$ can become large and negative (as shown in Fig. 16). This occurs at the centre of the droplet for χ_2 just less than 1.5 and at all locations for χ_2 close to zero. The

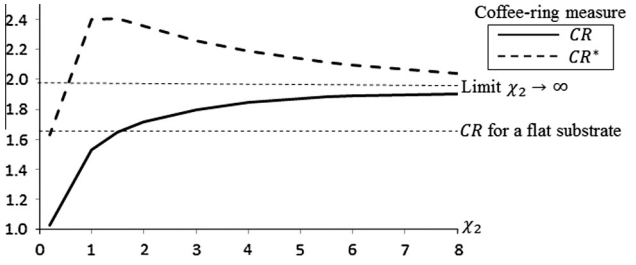

Fig. 13. The coffee-ring measure CR for the final $\bar{h}(\bar{r})$ profile as a function of the bank extent, χ_2. An analogous coffee-ring measure, $CR^\star$, is applied to the final $\bar{h}(\bar{r}) + \bar{\alpha}(\bar{r})$ profile and the results are superimposed for comparison. The results are shown for $Ca = 10^{-3}$, $f_h = 1$, $Pé \to \infty$, $\phi_0/\phi_{\max} = 0.4$ and $\chi_1 = 1/3$.

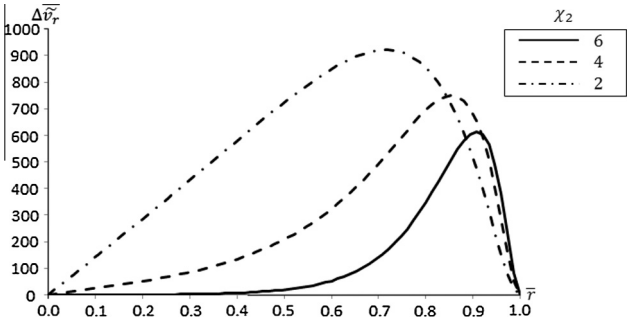

Fig. 14. A plot of the analytical expression for $\Delta\tilde{\bar{v}}_r$, as a function of the bank extent, χ_2 for $\chi_2 \geqslant 2$. The plots are shown for $Ca = 10^{-3}$, $g(\phi) = 1$, $\bar{h}(\bar{r}) = (1 + \chi_1) - \bar{\alpha}(\bar{r}) - \bar{r}^2$ and $\chi_1 = 1/3$. A positive $\Delta\tilde{\bar{v}}_r$ corresponds to an increase in the outward horizontal velocity.

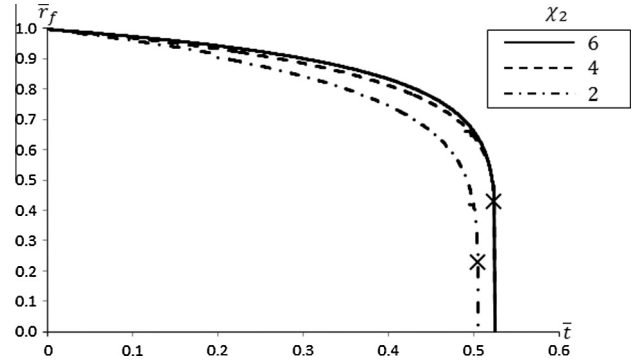

Fig. 15. The progression of the liquid/gel front location, $\bar{r}_f$, as a function of time and the bank slope, χ_2. The symbol $\times$ indicates the position of the original liquid/gel front when the droplet starts to gel at the centre as well. The results are shown for $Ca = 10^{-3}$, $f_h = 1$, $Pé \to \infty$, $\phi_0/\phi_{\max} = 0.4$, $\chi_1 = 1/3$ and the fixed shape initial condition.

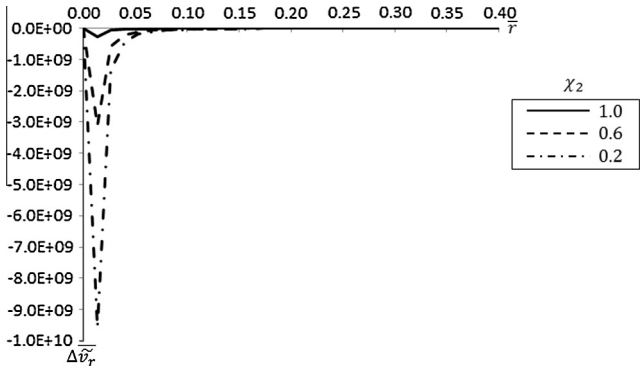

Fig. 16. A plot of the analytical expression for $\Delta\tilde{\bar{v}}_r$, as a function of the bank extent, χ_2 for $\chi_2 < 1$. The plots are shown for $Ca = 10^{-3}$, $g(\phi) = 1$, $\bar{h}(\bar{r}) = (1 + \chi_1) - \bar{\alpha}(\bar{r}) - \bar{r}^2$ and $\chi_1 = 1/3$. A negative $\Delta\tilde{\bar{v}}_r$ corresponds to a decrease in the outward horizontal velocity.

outward horizontal velocity is reduced and the coffee-ring formation becomes less extreme for both the $\bar{h}(\bar{r})$ profile and the $\bar{h}(\bar{r}) + \bar{\alpha}(\bar{r})$ profile, in the range $0 < \chi_2 < 1.5$.

For lower values of χ_2, the height of the droplet surface above the substrate decreases. It will thus take a shorter time for the polymer volume fraction to reach the gelation point. The outward capillary flow causing the coffee-ring effect has a shorter period of time to act before the height becomes fixed. This mechanism can also contribute to the reduction in CR.

It is to be noted that a trough with $0 < \chi_2 \leqslant 1.5$ may not be appropriate for printing in P-OLED applications.

3.3. A central raised trough basin

To demonstrate how the model can be used to investigate the influence of the substrate on film shape, for arbitrary geometry, we consider a raised central region in the trough basin such that

$$\bar{\alpha}(\bar{r}) = \chi_1 \cdot \left[\tanh^{-1}(\bar{r} \cdot \tanh(1))\right]^{\chi_2} + \frac{1 - \cos(5\bar{r})}{80\bar{r}^2} \quad \text{for } 0 < \bar{r} < 1 \tag{25}$$

Fig. 17 shows the substrate geometry compared to a substrate with a centrally flat trough basin, for $\chi_1 = 1/3$ and $\chi_2 = 6$.

Fig. 18 shows the final $\bar{h}(\bar{r})$ and $\bar{h}(\bar{r}) + \bar{\alpha}(\bar{r})$ profiles in both cases, for $\chi_1 = 1/3$ and $\chi_2 = 6$.

The introduction of a centrally raised region in the trough basin causes a subtle change to the final $\bar{h}(\bar{r})$ profile. The centrally raised

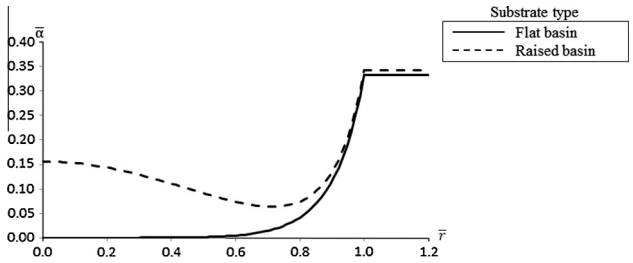

Fig. 17. Substrate profile $\bar{\alpha}(\bar{r})$ for a trough with the centrally raised basin, defined in Eq. (25) and the flat central basin, defined in Eq. (14). The profiles are shown for $\chi_1 = 1/3$ and $\chi_2 = 6$.

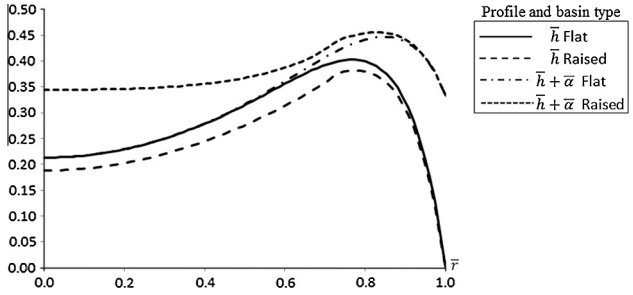

Fig. 18. The final $\bar{h}(\bar{r})$ and $\bar{h}(\bar{r}) + \bar{\alpha}(\bar{r})$ profiles for the substrate geometries plotted in Fig. 17. The results are shown for $Ca = 10^{-3}$, $f_h = 1$, $Pé \to \infty$, $\phi_0/\phi_{\max} = 0.4$, $\chi_1 = 1/3$, $\chi_2 = 6$ and the fixed shape initial condition.

region contributes to a larger outward flow and consequently the coffee-ring effect is slightly enhanced, when considering the measure *CR*.

There is a significant change to the $\bar{h}(\bar{r}) + \bar{\alpha}(\bar{r})$ profile when the centrally raised region is introduced. The centrally raised region reduces the coffee-ring effect, when considering an analogous measure to *CR* for the $\bar{h}(\bar{r}) + \bar{\alpha}(\bar{r})$ profile. This is due to the increased contribution of the substrate height at the centre.

The presence of a centrally raised region can also increase the likelihood of gelation occurring in the centre, in addition to the edge. When this occurs the height becomes fixed in the centre but can continue to decrease at other locations. In this eventuality the coffee-ring measure, *CR*, used previously might suggest an improvement to film shape. However, the final profile could be far from flat and so a more appropriate, situational dependent, measure for the film shape would need to be adopted.

4. Conclusion

A volatile droplet, containing polymer and residing on a geometrically patterned substrate was considered. This paper presented a theoretical investigation of how the substrates' geometrical properties impact the final shape of the polymer film. When a droplet is pinned, an area of enhanced deposition occurs, typically at the edge. This is termed the coffee-ring and is a result of an outward capillary flow that replenishes liquid material evaporated close to the edge.

The purpose of this paper was to identify substrate geometries that reduce the extent of the coffee-ring effect. We have extended a thin-film lubrication model [36] to account for a trough-like geometry, typically used in P-OLED displays. Rather than investigating the absolute height of the final film, we concentrate on the final height above the substrate, pertinent for our application. Literature devoted to considering this problem is very limited. Okuzono et al. [33] exclusively considered rectangular troughs, with a cartesian coordinate system. We have confirmed the film shape trend with trough depth and elucidated the influence of the walls' slope, for non-rectangular troughs. Further, the mechanism that leads to these trends has been determined.

We find that the substrate profile can alter the internal flow within the droplet and hence change the resultant film shape. Increasing the depth of the trough, increases the amount of material deposited at the edge and reduces that remaining at the centre; the coffee-ring effect is increased. The reason for this is two fold. First, a greater film thickness takes a longer period of time to reach the gelation concentration. The outward capillary flow therefore acts for an extended period before the height gets fixed by the gelation process. Second, the outward flow can be enhanced by the incline of the trough. These two effects combine but typically the former is the dominant effect. For the same reasons, the coffee-ring effect becomes even more apparent if the slope of the trough walls is increased.

In the future, this work could be extended to introduce Marangoni flow [19], edge-enhanced evaporation profiles [16] and a second liquid component [37]. Consideration of smaller solids content should be possible, however, this situation is complicated by gelation occurring at the centre in addition to the edge [36,33]. The fundamental assumption of lubrication theory is not valid for thick droplets, in deep troughs. By relaxing this assumption, a complicated biaxial moving boundary problem would result. As we have demonstrated, other substrate geometries can be considered, for example, a substrate with a centrally raised region in the trough basin. In principle, the substrate shape could be optimised to achieve the desired film shape.

Acknowledgements

This research has been funded by the Engineering & Physical Sciences Research Council, UK and CASE studentship funding from Cambridge Display Technology Ltd., UK.

Appendix A. Supplementary material

Supplementary data associated with this article can be found, in the online version, at http://dx.doi.org/10.1016/j.jcis.2015.07.036. These data include MOL files and InChiKeys of the most important compounds described in this article.

References

[1] Y.Y. Tarasevich, I.V. Vodolazskaya, O.P. Bondarenko, Modeling of spatial-temporal distribution of the components in the drying sessile droplet of biological fluid, Colloids Surfaces A: Physiochem. Eng. Aspects 432 (2013) 99–103.
[2] D. Brutin, B. Sobac, C. Nicloux, Influence of substrate nature on the evaporation of a sessile drop of blood, J. Heat Transf. 134 (6) (2012) 061101.
[3] D. Brutin, B. Sobac, B. Loquet, J. Sampol, Pattern formation in drying drops of blood, J. Fluid Mech. 667 (2011) 85–95.
[4] T. Heim, S. Preuss, B. Gerstmayer, A. Bosio, R. Blossey, Deposition from a drop: morphologies of unspecifically bound DNA, J. Phys.: Condens. Matter 17 (9) (2005) S703–S715.
[5] P. Angenendt, Progress in protein and antibody microarray technology, Drug Discov. Today 10 (7) (2005) 503–511.
[6] T. Goldmann, J.S. Gonzalez, DNA-printing: utilization of a standard inkjet printer for the transfer of nucleic acids to solid supports, J. Biochem. Biophys. Methods 42 (2000) 105–110.
[7] Y. Deng, X.Y. Zhu, T. Kienlen, A. Guo, Transport at the air/water interface is the reason for rings in protein microarrays, J. Am. Chem. Soc. 128 (9) (2006) 2768–2769.
[8] S. Basi, M. Hunsche, G. Noga, Effects of surfactants and the kinetic energy of monodroplets on the deposit structure of glyphosate at the micro-scale and their relevance to herbicide bio-efficacy on selected weed species, Weed Res. 53 (1) (2013) 1–11.
[9] H. Sirringhaus, T. Kawase, R.H. Friend, T. Shimoda, M. Inbasekaran, W. Wu, E.P. Woo, High-resolution inkjet printing of all-polymer transistor circuits, Science 290 (5499) (2000) 2123–2126.

[10] D. Kim, S. Jeong, B. Park, J. Moon, Direct writing of silver conductive patterns: improvement of film morphology and conductance by controlling solvent compositions, Appl. Phys. Lett. 89 (2006) 264101-1–264101-3.
[11] T. Sekitani, Y. Noguchi, U. Zschieschang, H. Klauk, T. Someya, Organic transistors manufactured using inkjet technology with subfemtoliter accuracy, PNAS 105 (13) (2008) 4976–4980.
[12] B.Y. Ahn, E.B. Duoss, M.J. Motala, X. Guo, S.I. Park, Y. Xiong, J. Yoon, R.G. Nuzzo, J.A. Rogers, J.A. Lewis, Omnidirectional printing of flexible, stretchable, and spanning silver microelectrodes, Science 323 (5921) (2009) 1590–1593.
[13] M. Naqshbandi, J. Canning, B.C. Gibson, M.M. Nash, M.J. Crossley, Room temperature self-assembly of mixed nanoparticles into photonic structures, Nat. Commun. 3 (2012) 1188-1–1188-7.
[14] Y. Jung, T. Kajiya, T. Yamaue, M. Doi, Film formation kinetics in the drying process of polymer solution enclosed by bank, Jpn. J. Appl. Phys. 48 (2009) 031502.
[15] B.J. de Gans, U.S. Schubert, Inkjet printing of well-defined polymer dots and arrays, Langmuir 20 (18) (2004) 7789–7793.
[16] R.D. Deegan, O. Bakajin, T.F. Dupont, G. Huber, S.R. Nagel, T.A. Witten, Capillary flow as the cause of ring stains from dried liquid drops, Nature 389 (1997) 827–829.
[17] R.D. Deegan, Pattern formation in drying drops, Phys. Rev. E 61 (1) (2000) 475–485.
[18] R.D. Deegan, O. Bakajin, T.F. Dupont, G. Huber, S.R. Nagel, T.A. Witten, Contact line deposits in an evaporating drop, Phys. Rev. E 62 (1) (2000) 756–765.
[19] T. Kajiya, W. Kobayashi, T. Okuzono, M. Doi, Controlling the drying and film formation processes of polymer solution droplets with addition of small amounts of surfactants, J. Phys. Chem. B 113 (2009) 15460–15466.
[20] A.W. Wray, D.T. Papageorgiou, R.V. Craster, K. Sefiane, O.K. Matar, Electrostatic suppression of the coffee-stain effect, Langmuir 30 (20) (2014) 5849–5858.
[21] R. Bhardwaj, X. Fang, P. Somasundaran, D. Attinger, Self-assembly of colloidal particles from evaporating droplets: role of DLVO interactions and proposition of a phase diagram, Langmuir 26 (11) (2010) 7833–7842.
[22] V.R. Dugyala, M.G. Basavaraj, Control over coffee-ring formation in evaporating liquid drops containing ellipsoids, Langmuir 30 (29) (2014) 8680–8686.
[23] H.B. Eral, D. Mampallil Augustine, M.H.G. Duits, F. Mugele, Suppressing the coffee stain effect: how to control colloidal self-assembly in evaporating drops using electrowetting, Soft Matter 7 (2011) 4954–4958.
[24] J. Vermant, Fluid mechanics: when shape matters, Nature 476 (2011) 286–287.
[25] P.J. Yunker, T. Still, M.A. Lohr, A.G. Yodh, Suppression of the coffee-ring effect by shape-dependent capillary interactions, Nature 476 (2011) 308–311.
[26] R.G. Larson, Transport and deposition patterns in drying sessile droplets, AIChE J. 60 (5) (2014) 1538–1571.
[27] A.F. Routh, Drying of thin colloidal films, Rep. Progr. Phys. 76 (4) (2013) 046603-1–046603-30.
[28] K. Ozawa, E. Nishitani, M. Doi, Modeling of the drying process of liquid droplet to form thin film, Jpn. J. Appl. Phys. 44 (6A) (2005) 4229–4234.
[29] B.J. Fischer, Particle convection in an evaporating colloidal droplet, Langmuir 18 (1) (2002) 60–67.
[30] A.F. Routh, W.B. Russel, Horizontal drying fronts during solvent evaporation from latex films, AIChE J. 44 (9) (1998) 2088–2098.
[31] J.M. Salamanca, E. Ciampi, D.A. Faux, P.M. Glover, P.J. McDonald, A.F. Routh, A.C.I.A. Peters, R. Satguru, J.L. Keddie, Lateral drying in thick films of waterborne colloidal particles, Langmuir 17 (2001) 3202–3207.
[32] M.C. Lopes, E. Bonaccurso, Evaporation control of sessile water drops by soft viscoelastic surfaces, Soft Matter 8 (2012) 7875–7881.
[33] T. Okuzono, M. Kobayashi, M. Doi, Final shape of a drying thin film, Phys. Rev. E 80 (2009) 021603.
[34] B. Garcia, M.J. Miranda, J.M. Leal, J. Ortega, J.S. Matos, Densities and viscosities of mixing for the binary system of methyl benzoate with n-nonane at different temperatures, Thermochim. Acta 186 (1991) 285–292.
[35] I.M. Krieger, T.J. Dougherty, A mechanism for non-Newtonian flow in suspensions of rigid spheres, Trans. Soc. Rheol. 3 (1959) 137–152.
[36] A.D. Eales, N. Dartnell, S. Goddard, A.F. Routh, Evaporation of pinned droplets containing polymer – an examination of the important groups controlling final shape, AIChE J. 61 (5) (2015) 1759–1767.
[37] A.D. Eales, N. Dartnell, S. Goddard, A.F. Routh, Thin, binary liquid droplets, containing polymer: an investigation of the parameters controlling film shape, submitted for publication.